Improving the Performance of Perovskite Solar Cells with Insulating Additive-Modified Hole Transport Layers

Guodong Zhang, Yifan Zheng,* Yifeng Shi, Xiaorong Ma, Mengjie Sun, Tao Li, Bin Yang, and Yuchuan Shao*
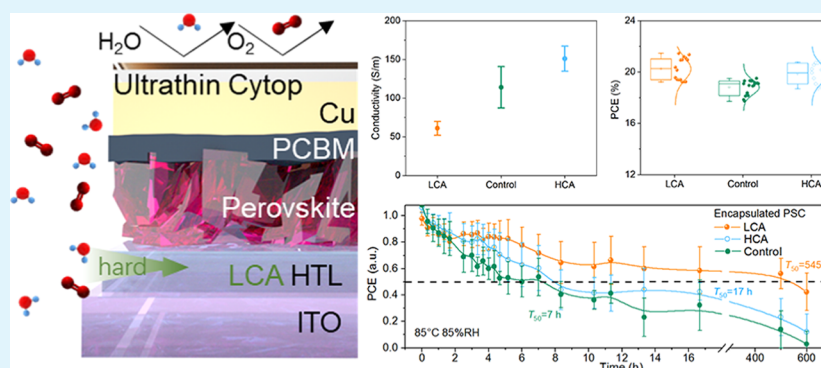
Read Online

ACCESS | Metrics & More | Article Recommendations | Supporting Information

ABSTRACT: Invert perovskite solar cells (PSCs) present a great potential for next-generation photovoltaics for their flexibility and tandem adaptability. In order to improve the conductivity of the hole transport layer (HTL), such as poly(triarylamine), highly conductive additives (e.g., F4TCNQ, Li-TFSI) were generally applied to achieve a power conversion efficiency (PCE) exceeding 21%. However, these additives significantly affect the long-term stability of the devices due to their humidity sensitivity. In this work, the HTL was counterintuitively optimized with insulating additives, such as polyphenylene sulfide, which enhanced PCE from 19.1 to 21.5% along with a noticeable improvement in device stability with T50 of 574 h under double 85 aging conditions. The performance enhancement is attributed to larger grain sizes in perovskite films on the HTL and better energy-level alignment between the HTL and perovskite after introducing the insulating additives, which compensate negative influence caused by additive-induced reduction in conductivity. Our work demonstrates that low-conductivity additives, rather than the commonly used high-conductivity counterparts, can also contribute to improving the photovoltaic performance in PSCs.

KEYWORDS: *perovskite solar cell (PSC), inverted PSC, hole transport layer (HTL), additives, conductivity*

■ INTRODUCTION

Inverted perovskite solar cells (PSCs), in which perovskites are fabricated on the top of the hole transport layer (HTL), have attracted universal attention, owing to their easy fabrication, cost-effectiveness, and suppressed hysteresis characteristics.[1−8] HTLs can not only separate the charges and transport the holes but also determine the crystalline quality of the upper perovskites.[9,10] Compared with inorganic HTLs, organic HTLs with comparable hole mobility and lower processing temperature are more friendly to commercial PSCs.[11,12,42] Poly-(triarylamine) (PTAA), in particular, with excellent hole mobility and great stability at 85 °C, has been developed into the most widely used organic HTLs in the state-of-the-art inverted PSCs with power conversion efficiencies (PCEs) over 21%.[13−15,39−41] However, PTAA is likely to form high-energy disorder and poor $\pi-\pi$ interactions due to its long and distorted backbone triphenylamine.[16−18] Additive engineering has been proven to be a simple and effective way to modify the

PTAA HTL, in which p-type additives with relatively high conductivity are usually be used.[19] As early as 2006, Grätzel et al. introduced Li-TFSI additives in dye-sensitized solar cell (DSSC).[20] Subsequently, in PSCs, the effect of Li-TFSI in PTAA was explored, which resulted in a significant increase in the film conductivity.[21] Then, in 2015, the introduction of F4TCNQ into PTAA was informed by Huang et al., in which significant increase in PTAA conductivity was found.[22] After that, studies of chemical additive effects have associated the enhancement of the device PCE to the increased conductivity of PTAA.[23,24]
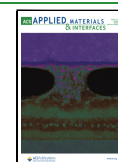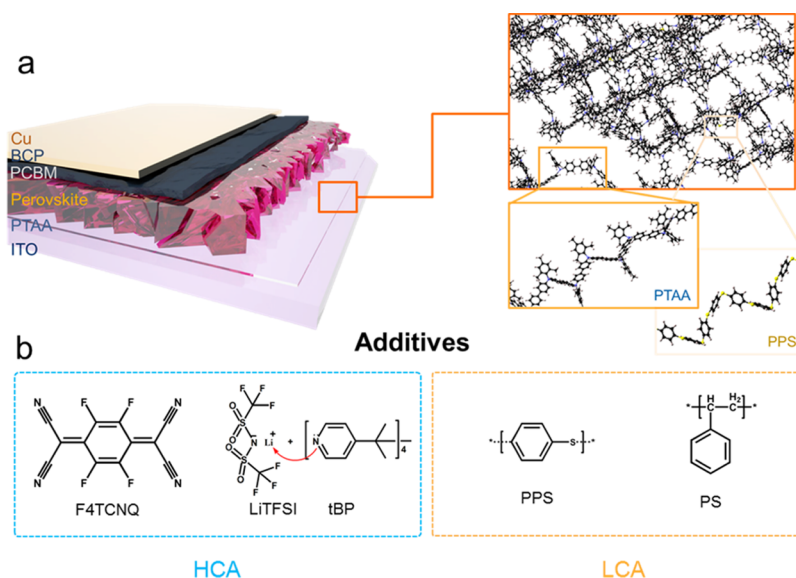
Figure 1. Schematic diagram and conductivity test in this work. (a) Device structure and schematic diagram of HTL additive engineering. (b) Molecular structure of additives used in this work.

However, recent state-of-the-art PSCs are favored to employ additive-treated ultrathin PTAA to achieve more efficient light absorption and charge extractions. Generally, ultrathin HTLs with few nanometers are often discontinuous, in which perovskite absorbers may direct contact with the bottom indium tin oxide (ITO) electrode.[12,13,25,26] In this case, holes could be directly extracted without passing through the HTL. It is not justified to directly attribute the PCE enhancement to the increased HTL conductivity. In addition to the unclear mechanism, additives could greatly affect the long-term stability of the PSC.[27] The ultra-sensitive nature of some p-type additives to humidity will accelerate the decomposition of perovskite.[28,29] Moreover, the distribution of additives affects the crystalline nature and film morphology of PTAA, resulting in a massive variation in the device performance.[22] Therefore, it is necessary to clarify the relationship between HTL additives and device performance improvement, paving the route for future commercial PSCs with high efficiency and stability. Unfortunately, a fundamental understanding of these has yet to be achieved.

Here, we uncover the additive mechanism using the additives with different conductivity. Counterintuitively, PSCs with insulating additive-modified HTL obtain the highest performance. Further investigation revealed that the better crystalline growth of perovskite on the HTL is crucial to the device PCE, rather than the conductivity variations of the HTL induced by additives. Ultimately, through optimization, we increased the device PCE from 19.1 to 21.5% and observed a noticeable enhancement in device stability with T_{50} of 574 h under double 85 aging conditions.

RESULTS AND DISCUSSION

The planar heterojunction perovskite solar cells in this work were structured as ITO/PTAA/perovskite/[6,6]-phenyl C_{61} butyric acid methyl ester (PC$_{61}$BM)/2,9-dimethyl-4,7-diphenyl-1,10-phenanthroline (BCP)/copper (Cu), as shown in Figure 1a. Here, the specific composition of perovskite is Cs$_{0.05}$(FA$_{0.84}$MA$_{0.16}$)$_{0.95}$Pb(I$_{0.84}$Br$_{0.16}$)$_3$. To examine the effects of HTL conductivity on the PSC performance, we use several additives with various conductivity. Based on the additives'

conductivity, we separated HTL additives into low-conductivity additives (LCAs) and high-conductivity additives (HCAs). For LCA, insulation materials with low conductivity include polystyrene (PS) and polyphenylene sulfide (PPS). For HCA, F4TCNQ and Li-TFSI (tBP) are selected. The chemical structure of additives used in this work is shown in Figure 1b.

We fabricate the PSC to study the effects of HTL additives on the device performance. It is unexpected to find that LCA PSCs could obtain higher PCE than HCA PSCs (the initial experimental results are shown in Figure S1 and Table S1). The statistical data are collected from 30 pieces of PSCs, indicating that the phenomenon of abnormal high PCE for LCA-based PSCs is reliable. It is worth proposing that Li-TFSI (tBP) additive could affect the perovskite formation (visual observation shows that the film is rough and yellowing easily) due to the hydrophilicity of Li-TFSI, leading to wide device performance variations. For more detailed study and optimization, in the following, we chose PPS and F4TCNQ for the comparison (presented as LCA and HCA, respectively). As shown in Figure 2a, LCA could provide a PCE over 20%, better than control and HCA devices. From statistical data in Figure 2b, we observed that the short current density (J_{SC}) of the HCA is higher than that of LCA. This is consistent with the previous HTL studies, in which the improvement of HTL conductivity benefits the charge extraction. In contrast, LCA PSCs with comparable J_{SC} and significantly enhanced fill factor (FF) give rise to the highest PCE (Figure 2c).

We obtained the champion devices by optimizing the concentration of PPS and F4TCNQ in PTAA solution as 0.015 and 0.01 mg/mL, respectively. Current density–voltage (J–V) curves of champion PSCs are presented in Figure 2d (parameter details are listed in Table S2). The control PSC obtains the best PCE of 19.1%, with a V_{OC} of 1.14 V, a J_{SC} of 22.4 mA/cm^2, and a FF of 75%. In contrast, the LCA HTL-based device delivers an optimal PCE of 21.5%, with a V_{OC} of 1.16 V, a J_{SC} of 22.6 mA/cm^2, and a FF of 82%. The HCA HTL-based PSC delivers a champion PCE of 20.5%, a V_{OC} of 1.15 V, a J_{SC} of 23.3 mA/cm^2, and a FF of 77%. The integrated J_{SC} values obtained from the external quantum efficiency (EQE) agree closely with J_{SC} extracted from J–V curves
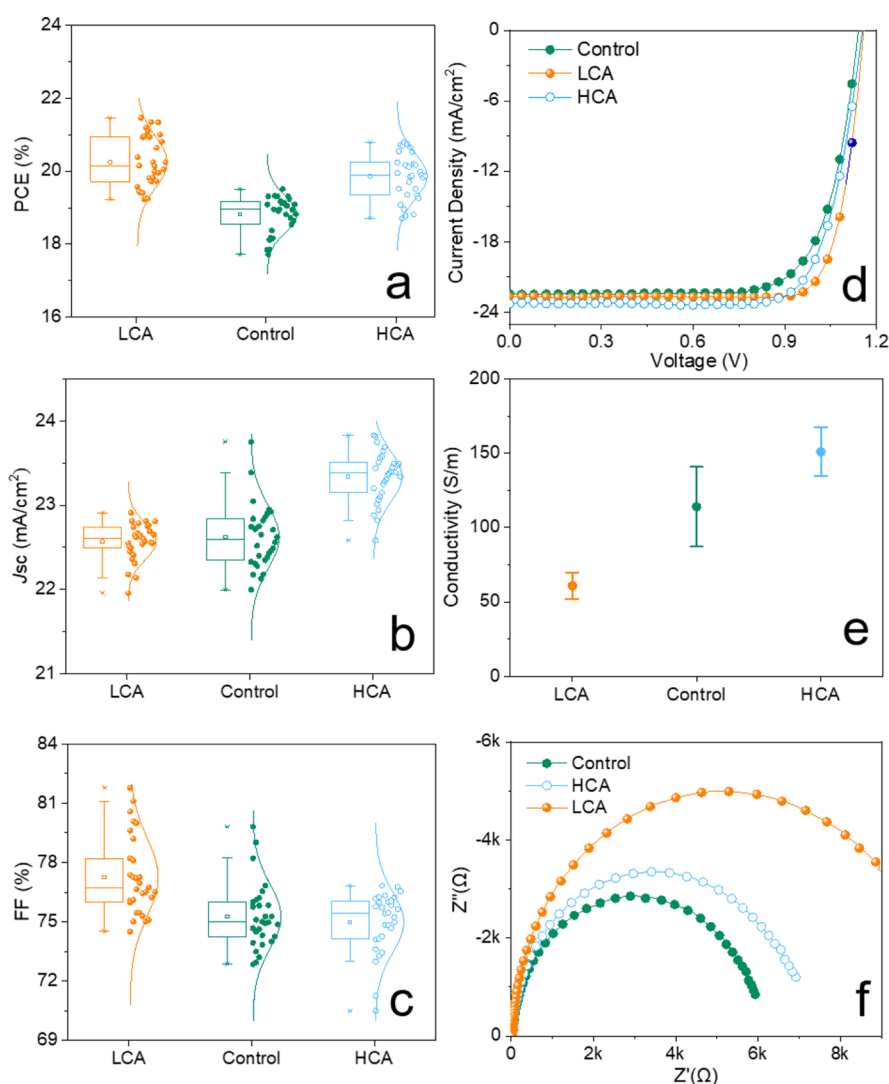
Figure 2. PSC photovoltaic performance. (a−c) Statistical data of PCE, J_{SC}, and FF collected from the 30 devices, respectively. (d) $J−V$ curves of the champion devices based on control (green), LCA (PPS) (orange), and HCA (F4TCNQ) (blue) HTLs, respectively. (e) Conductivity of HTLs (details are shown in Figure S3). (f) Nyquist plot of devices, measured under dark conditions, with 0.9 V bias voltage and 1 MHz to 20 Hz scanning range (fitting curves are presented in Figure S4).

(Figure S2a). The $J−V$ curves under reverse and forward scans are presented in Figure S2b (parameter details are listed in Table S3). Low $J−V$ hysteresis for LCA PSCs with the declined hysteresis index, from 0.06 to 0.04, indicates hindered defects in the perovskite interface or bulk.[30−32] Besides, we further investigate the operational stability of the PSCs by aging the unencapsulated devices under a nitrogen atmosphere, using maximum-power-point (MPP) tracking under 1-sun illumination (Figure S2c). Stabilized PCEs of 16.8, 20.4, and 16.9% are shown for the PSCs based on control, LCA, and HCA HTLs, respectively. The LCA device exhibits the best stability performance, whereas the HCA PSC presents an obvious decay after 900 s MPP tracking.

Subsequently, we applied resistance measurement to better understand the HTL conductivity variations. We first test the conductivity of HTLs by measuring the $I−V$ characteristic of devices with a simple configuration of ITO/HTL/Cu (Figure 2e).[33,34] Concentration of additives in PTAA is the same as those used in the champion PSCs (Table S1). The conductivity of HTLs has been calculated to be 61 and 151 S/m for LCA and HCA, respectively (the control HTL shows

the conductivity of 113 S/m). We also perform conductive atomic force microscopy (C-AFM) to verify the change in conductivity (Figure S4). The result is consistent with $I−V$ characteristics. As expected, the conductivity of HTL largely depends on the additives' conductivity, in which insulation materials result in the lowest HTL conductivity. To accurately measure the device resistance, impedance spectroscopy (IS) was used. Nyquist plots of the device based on different HTLs are presented in Figure 2f (fitting curves are plotted in Figure S5, and parameters details are listed in Table S4). In our case, only one semicircle can be observed, suggesting that the quasi-Ohmic contacts dominated in the interface rather than rectifying contacts. In general, resistance at a low frequency is mainly associated with interfacial charge recombination, whereas charge-transfer contact responses for the resistance at a high frequency.[35] The equivalent circuit consists of two interfacial resistances, which are related to charge transport resistance (R_{ct}) and charge recombination resistance (R_{rec}), respectively (Figure S5a).[37,43] At a high frequency, we find that the difference in R_{ct} between various PSCs is negligible (Table S4). In our case, an ultrathin HTL may form a discontinuous
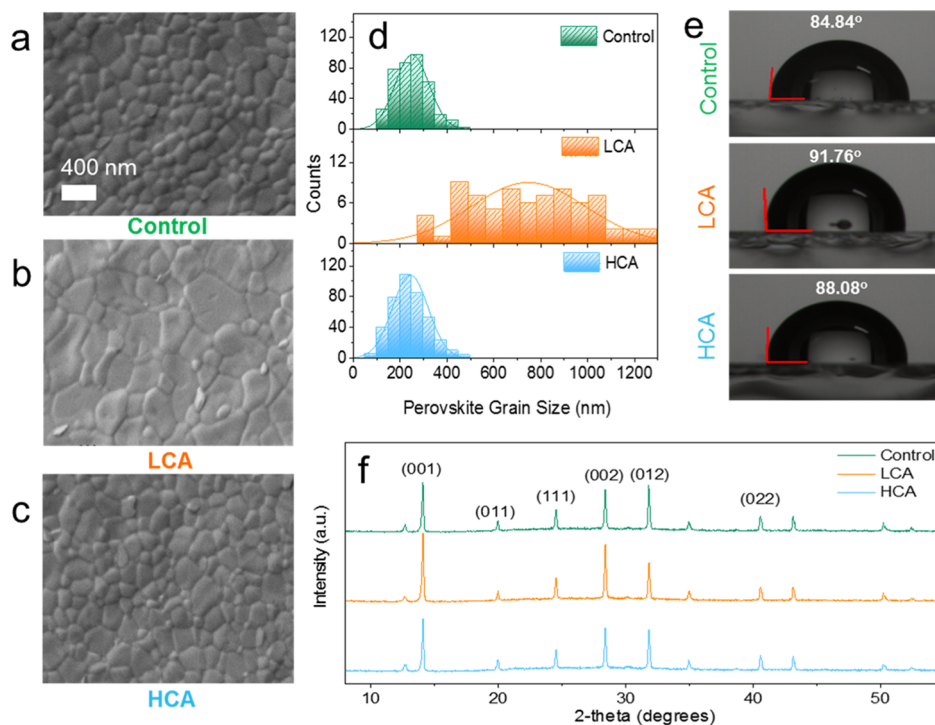
Figure 3. Morphology and crystallinity characterizations. SEM images of perovskite films based on different HTLs: (a) control, (b) LCA, and (c) HCA. (d) Statistical distribution of perovskite grain size. (e) Contact angle images of control, LCA, and HCA, respectively. (f) XRD patterns of the perovskite grown on different HTLs.

film. Hence, it is important to note that the HTL conductivity has no direct relation to the series resistance. At a low frequency, the LCA device demonstrates a R_{rec} of 10,255 Ω, which is much larger than the control (5679 Ω) and HCA (6704 Ω), revealing the hindered carrier recommendation rate. The retrieval time constant, τ, corresponding to the charge recombination, for LCA (47.3 μs) is about twice that of HCA (31.9 μs) and control (26.5 μs) (Table S4). We also perform thermal admittance spectroscopy (TAS) to investigate the defect trap density (Figure S5b). The shallow trap region (0.30−0.40 eV) and deep trap region (0.40−0.55 eV) are assigned to traps at grain boundaries and defects at the film surface, respectively.[35] The TAS results indicate a significant reduction in bulk defects and a noticeable decrease in surface defects for LCA PSCs. These results prove that the better crystalline quality of perovskite grown on the LCA HTL has retarded defects at the bulk and interface.

To future explore the reason for the high PCE of LCA devices, we use atomic force microscopy (AFM) to measure the morphology changes (Figures S6, S8). The pores in the LCA and HCA PTAA decrease considerably compared with control PTAA. The roughness of HCA HTL is larger than LCA HTL, which could be attributed to the agglomeration phenomenon of F4TCNQ. Although the HTL morphology obtains unconsidered changes, the morphology of upper perovskite films alters significantly through scanning electron microscopy (SEM) characterization. The grain size of the perovskite on control HTL is not uniformly distributed, and there are many small-sized crystals on the surface. By comparison, the grain size of the LCA perovskite is much larger than that of the control and HCA perovskite (Figure 3a−c). Based on the statistical analysis, we find that the LCA perovskite film has 2−3 times grain size larger than other films (Figure 3d). With larger crystalline grains, LCA perovskites

receive fewer grain boundaries and defects, thus strongly limit the carrier recombination. This is consistent with the results of impedance analysis and PSC performance. The contact angle measurement was further used to study the surface wettability of HTLs. The control HTL exhibits a contact angle of 84.8°. The contact angle rises to 91.8 and 88.1° for LCA and HCA HTLs, significantly. As illustrated previously, a non-wetting surface can increase nucleus spacing by suppressing the heterogeneous nucleation and facilitating the grain boundary migration in grain growth by imposing less drag force.[26] Especially among high contact angle range, a few degrees difference can cause two to three times large grain size.[26] In this case, the LCA PSC obtains obvious large perovskite grain, resulting in fewer grain boundaries and restricted defects (Figure 3b). To reveal the variation of the crystal structure of perovskite films, we perform X-ray diffractograms (XRD) (Figure 3f). The perovskite films exhibit a preferential orientation accompanied by the appearance of two diffraction peaks at the angles 14.1 and 28.4°, corresponding to the (001) and (002) lattice planes. Notably, the (001) and (002) peaks of LCA are stronger than that of the other samples, suggesting that a better crystal quality for perovskite crystalline was obtained on the LCA HTL, which is also consistent with SEM results. To examine the band gap variations of the perovskite, we measured the optical absorption spectra of perovskite films by ultraviolet−visible (UV−vis) spectroscopy (Figure S7). It was found that there are almost no differences between control and doped HTL, which means that the HTL only promotes the perovskite crystalline quality without changing its band gap (estimated to be 1.63 eV from Tauc-plot results).

To investigate the charge-transfer mechanism between perovskite films and HTLs, we present kelvin probe force microscopy (KPFM) at first. The work function fluctuation of HTLs could be determined by the potential difference between
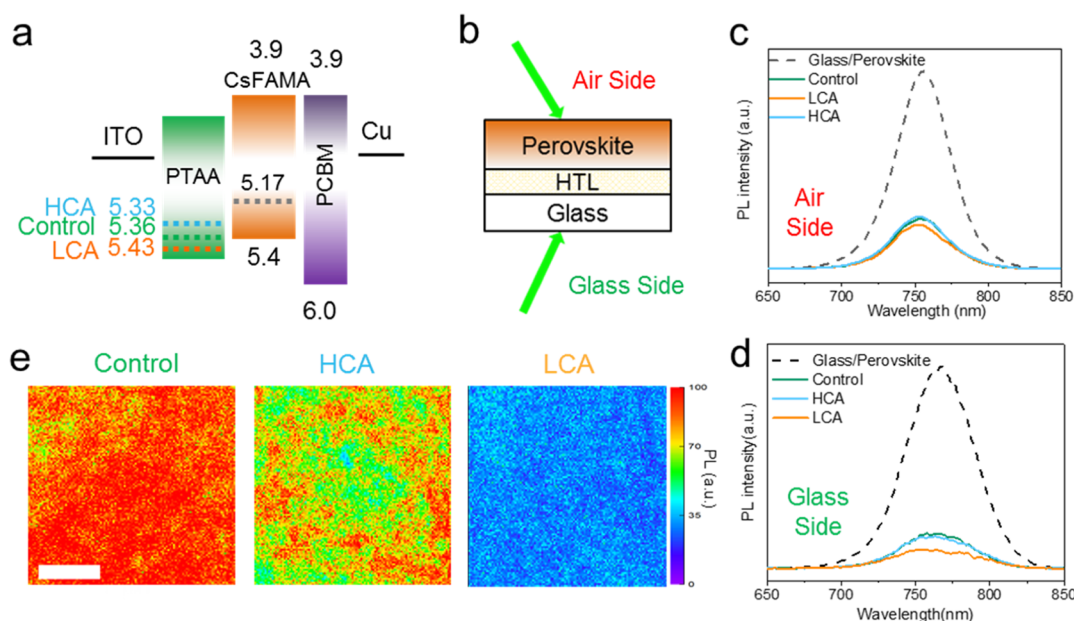
Figure 4. Charge transport mechanism. (a) Energy diagrams of PSCs based on the results of KPFM (Figure S6). (b) Experiment setup for steady-state PL. (c) PL spectra for devices with 405 nm excitation incident from the air side: glass/perovskite (black), control (green), LCA (orange), and HCA (sky blue). (d) PL spectra for devices with 405 nm excitation incident from the glass side: glass/perovskite (black), control (green), LCA (orange), and HCA (sky blue). (e) PL mapping of perovskite films deposited on different HTLs with a scale bar of 1 μm.
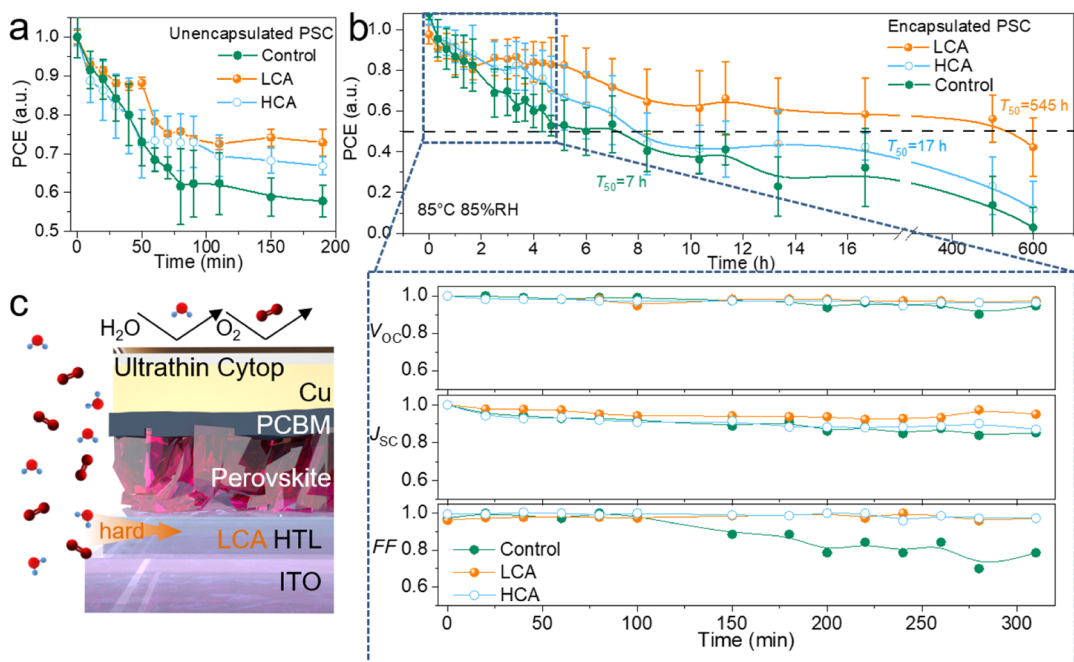

Figure 5. Device stability under double 85 aging condition. (a) PCE stability of the unencapsulated devices. (b) PCE, V_{OC}, J_{SC}, and FF stability of the encapsulated devices. Enlarge box shows the decayed device performance within the first 300 min. (c) Description of the stability enhancement mechanism: insulator additives fill the pin-hole of PTAA films, thus retarding the penetration of oxygen and water molecular from air ambient, contributing to the greatly enhanced device stability.

the gold area and the PTAA area.[36] The geometry of the KPFM measurements is illustrated in Figure S8. The additives might tune the work function of HTL, resulting in the charge extraction difference. Referring to the previous study, we vapored the strip gold electrodes as a work function reference.[14,23] A large contact potential difference (CPD) is observed between gold area and PTAA area. The CPD in the measurements is defined as $(\varphi_{tip} - \varphi_{sample})/e$. We use the same conductive tip; thus, the CPD value should be directly related

to the work function of the measured samples. As shown in Table S5, the CPD of the control, LCA, and HCA PTAA films and CsFAMA perovskite films were 0.26, 0.23, 0.33, and 0.07 V lower than that of Au. Therefore, the Fermi energy levels of HTLs and perovskite films were calculated as 5.33 eV (HCA), 5.36 eV (control), 5.43 eV (LCA), and 5.17 eV (CsFAMA perovskite films), respectively (Figure 4a). The larger Fermi energy level difference between HTLs and perovskite means a larger energy band bending, which also signifies a larger built-

in electric field and more efficient charge extraction. These small differences in the Fermi energy level would not significantly impact the device hole extraction.

Furthermore, we carried out the steady-state photoluminescence (PL) measurement to explore the charge-transfer mechanism. Excitation light of 405 nm was chosen because it has a much lower penetration length than the thickness of perovskite films.[37] We varied the excitation place on both sides of the perovskite film (Figure 4b). As it is well known, better perovskite crystalline quality and higher hole extraction efficiency at the perovskite/HTL interface contribute to the stronger PL quenching. As shown in Figure 4c,d, the HTL-free perovskite films exhibit a strong PL at 755 nm, regardless of the direction of excitation light incidence, which means that the top and bottom surfaces have the same optical property. When the HTL is applied, significant PL quenching occurs, indicating that the holes can be extracted efficiently in the PTAA HTL system. This efficient hole extraction makes PTAA a widely used HTL for the preparation of high-efficiency inverse PSCs. No obvious PL quenching difference was found whether the incident light was from the glass side or the air side, indicating the negligible difference in charge extraction ability among these HTLs. For a more intuitive presentation, we presented PL mapping (Figure 4e). We noted that inhomogeneous PL intensity was observed for the HCA perovskite, suggesting that F4TCNQ was non-uniform distribution in the PTAA. The green region in the PL mapping plot is due to the enrichment of F4TCNQ in the HTL, while the red region corresponds to the area with less hole extraction efficiency. In contrast, LCA exhibits more homogeneous PL intensity, associated with the promoted perovskite crystalline quality and uniform distribution of additives. Therefore, we can conclude that the variation in charge extraction capacity induced by the different conductivity of the ultrathin HTL is negligible, and we should pay more attention to the crystal quality of the perovskite film.

Long-term device stabilities during operation under stressed conditions such as ambient air, elevated temperature, and under light illumination are all critical for the commercialization of PSCs.[44−46] The double 85 aging condition (85 °C, 85% RH) is one of the important criteria to judge the stability and commercialization possibility of the PSCs.[37] We performed the stability test under double 85 aging conditions, where PSCs with or w/o capsulation were kept for testing (Figure 5a,b). For better observation of top electrode changes, we used ultrathin Cytop for capsulation without applying seal glass on the top, as illustrated in Figure 5c.[38] We also took optical photographs of the device under double 85 conditions to observe the damage process (Figure S9). Without encapsulation, the LCA devices still maintain 74% of their initial efficiency at 190 min, while the HCA and control devices have obtained an obvious decay in PCE to 66 and 57%, respectively. As shown in Figure S9, the damages of Cu electrodes and the perovskite surface are mainly responsible for device degradation. Large grain size and crystalline quality contribute to the better stability of LCA devices at unencapsulated conditions. With encapsulation, the electrodes and surface perovskites are protected from top-to-bottom humidity penetration. In this case, the hydrophobicity and stability of HTL become the primary responsibility to the devices lifetime. As shown in Figure S9, the electrodes and upper surface of the packaged device have negligible change. The LCA PSCs have notably T_{50} (the time it takes for PCE to drop to half of its initial) of

574 h, while control and HCA only reveal a T_{50} of 7 and 13 h, respectively. The PTAA HTL has a porous surface (Figure S6), which water and oxygen molecular are able to penetrate through. As depicted in Figure 5b, without additives, the FF of the control PSC decreases significantly, indicating that the phase transition or perovskite decomposition mainly happens at the interface contacted between the HTL and perovskite. Additives could occupy these pores and thus protect the upper perovskite absorbers from direct contact with penetrated water molecules (Figure 5c). As shown in Figure S8, the pores in the LCA and HCA PTAA decrease considerably compared with control PTAA. The containment of high water-resisted insulator polymers among the pores could hence improve the hydrophobic properties of the porous PTAA film. For both LCA and HCA, FF can be maintained over 90% during the first 300 min under double 85 aging conditions. F4TCNQ has good hydrophobic properties because of the containment of F atom. Therefore, it is not difficult to understand the better stability of HCA-modified PSCs than control. In contrast, the insulation additives used for LCA have intrinsic advantages in terms of stability and water resistance, thus greatly improving the perovskite stability. This also consists of the ignorable change in colors after testing for 48 h, from both front and back observation (Figure S9). It is worth noting that the high temperature is the main reason for the decreased performance, which may lead to the phase transition or ion migration of the perovskite. Further study should focus on exploring the additives with good thermal insulation properties.

■ CONCLUSIONS

In summary, we obtain a significant PCE improvement from 19.1 to 21.5% by introducing insulating additives into the HTL. Further investigation reveals that LCA additives could modify the HTL surface contact without sacrificing its electrical properties, in which larger grain size, improved crystalline quality, and balanced charge extraction ratio are achieved. In addition, LCA can prevent the perovskite interface from the ambient humidity penetration, leading to great improvement in the devices long-term stability with T_{50} of 574 h. Our work will contribute to a more comprehensive understanding of HTL additive engineering, paving the way for facile access to approaching their commercial ambitions.

■ EXPERIMENTAL SECTION

Materials. Lead iodide (PbI$_2$), lead (II) bromide (PbBr$_2$), CH$_3$NH$_3$Br (MABr), NH$_2$CH═NH$_2$I (FAI), cesium iodide (CsI), PTAA, PC$_{61}$BM, and BCP were purchased from Xi'an Polymer Light Technology Corp. Dimethylformamide (DMF, 99.8%), dimethyl sulfoxide (DMSO, 99.9%), chlorobenzene (CB, 99.8%), and all of the additives were purchased from Sigma-Aldrich (USA). ITO-coated glass substrates (15 Ω·sq^{-1}) were purchased from South China Science & Technology Co. Ltd. (China). The above materials were used directly without further purification. For Li-TFSI (tBP) additives, Li-TFSI and tBP were mixed at a mole ratio of 1:2. PC$_{61}$BM solution was prepared by dissolving PC$_{61}$BM into CB with a concentration of 20 mg/mL and stirred at 60 °C overnight in the glovebox. The Cs$_{0.05}$(FA$_{0.84}$MA$_{0.16}$)$_{0.95}$Pb(I$_{0.84}$Br$_{0.16}$)$_3$ precursor solution was made by dissolving 172 mg of FAI, 507 mg PbI$_2$, 22.4 mg MABr, and 73.4 mg PbBr$_2$ (1:1.1:0.2:0.2 mole ratio) and 40 μL of CsI stock solution (1.5 M in DMSO) in 627 μL of DMF and 157 μL of DMSO (4:1 v/v) and stirring at 60 °C for 30 min.

Device Fabrication. ITO glasses were cleaned using the ultrasonic cleaner using diluted detergent, deionized water, acetone, and IPA, respectively. Before spin coating, ITO is treated with an UVO cleaner for 10 min. PTAA solution was prepared by dissolving

PTAA powder into CB with a concentration of 15 mg/mL with various concentration of additives from 0.01 to 0.05 mg/mL and stirred at 60 °C for 6 h. PTAA was spin-coated on ITO at 4000 rpm for 60 s and annealed at 100 °C for 10 min. After cooling to room temperature, the perovskite precursor was spin-coated on the HTLs first at 1000 rpm for 10 s and then at 4000 rpm for 50 s. Before the first step, 60 μL of DMF was dripped on the PTAA films. During the second step, 130 μL of CB was dripped on the top of the perovskite film 5 s prior to the end of the program. The perovskite film was then annealed at 100 °C for 15 min. After the substrate cooled to room temperature, $PC_{61}BM$ solution (20 mg/mL in CB) was spin-coated on perovskite films at 2000 rpm for 30 s. After that, 8 nm BCP and 80 nm Cu were deposited by thermal evaporation using a metal shadow mask. The device area was 0.08 cm^2.

Characterization. The current density−voltage (J−V) characteristics of the photovoltaic devices were measured using a computer-controlled Keithley 2400 sourcemeter. The characterization was performed in a N$_2$ glovebox under a simulated AM 1.5G solar illumination (100 mW/cm^2) with an Enlitech SS-F5S solar simulator. J−V scans were taken from forward bias to reverse bias with the following scan parameters: step size, 10 mV. EQE measurements were taken using an Enlitech QE-R. SEM was characterized by focused ion beam-SEM(Carl Zeiss AURIGA Cross-Beam). PL and TRPL spectra were measured at room temperature using a laser-scanned fluorescence lifetime/intensity imaging system (FLRM300, Time-Tech Spectra, LLC) with a 405 nm picosecond pulsed diode laser as an excitation source. The IS measurement was performed using a LCR meter (TH2826)..

■ ASSOCIATED CONTENT

Ⓢ Supporting Information

The Supporting Information is available free of charge at https://pubs.acs.org/doi/10.1021/acsami.1c24349.

> Time constant τ calculation of IS and TAS; photocurrents for the initial devices with control, LCA-1 (PPS), LCA-2 (PS), HCA-1 (F4TCNQ), HCA-2 (LiTSFI and tBP) HTLs; EQE of the LCA HTL-based PSCs; J−V curves of devices with control and LCA HTLs by forward and reverse scans; steady-state output at MPP of the corresponding unsealed devices; I−V characteristic of devices with a configuration of ITO/HTL/Cu; C-AFM of devices with a configuration of ITO/HTL; fitting curves of IS of PSCs and trap density of states obtained by thermal admittance spectroscopy; AFM images of HTLs: control, LCA, and HCA; absorption spectra of perovskite films coated on control, LCA, and HCA HTLs and Tauc-plot of perovskite films based on different HTLs; AFM and KPFM images of Au, control, HCA, and LCA; optical photographs of the device under double 85 conditions for 24 h without encapsulation and with ultrathin Cytop encapsulation; photovoltaic parameters of FAMAC PSCs; photovoltaic parameters obtained from the optimized devices; parameters of J−V curves of devices with control and LCA HTLs by forward and reverse scans; fitting parameters of IS; and statistical data of KPFM (PDF)

■ AUTHOR INFORMATION

Corresponding Authors

Yifan Zheng − *Key Laboratory of Materials for High-Power Laser, Shanghai Institute of Optics and Fine Mechanics, Chinese Academy of Sciences, Shanghai 201800, China; Center of Materials Science and Optoelectronics Engineering, University of Chinese Academy of Sciences, Beijing 100049,*

China; ⓘ orcid.org/0000-0002-8439-2245; Email: yifan.zheng@siom.ac.cn

Yuchuan Shao − *Key Laboratory of Materials for High-Power Laser, Shanghai Institute of Optics and Fine Mechanics, Chinese Academy of Sciences, Shanghai 201800, China; School of Physics and Optoelectronic Engineering, Hangzhou Institute for Advanced Study, UCAS, Hangzhou 310024, China; Center of Materials Science and Optoelectronics Engineering, University of Chinese Academy of Sciences, Beijing 100049, China;* ⓘ orcid.org/0000-0001-7155-456X; Email: shaoyuchuan@siom.ac.cn

Authors

Guodong Zhang − *Key Laboratory of Materials for High-Power Laser, Shanghai Institute of Optics and Fine Mechanics, Chinese Academy of Sciences, Shanghai 201800, China; Center of Materials Science and Optoelectronics Engineering, University of Chinese Academy of Sciences, Beijing 100049, China*

Yifeng Shi − *Key Laboratory of Materials for High-Power Laser, Shanghai Institute of Optics and Fine Mechanics, Chinese Academy of Sciences, Shanghai 201800, China*

Xiaorong Ma − *Center for Spintronics and Quantum Systems, State Key Laboratory for Mechanical Behavior of Materials, Department of Materials Science and Engineering, Xi'an Jiaotong University, Xi'an 710049, China*

Mengjie Sun − *School of Physics and Optoelectronic Engineering, Hangzhou Institute for Advanced Study, UCAS, Hangzhou 310024, China;* ⓘ orcid.org/0000-0003-0506-2721

Tao Li − *Center for Spintronics and Quantum Systems, State Key Laboratory for Mechanical Behavior of Materials, Department of Materials Science and Engineering, Xi'an Jiaotong University, Xi'an 710049, China*

Bin Yang − *College of Materials Science and Engineering, Hunan University, Changsha 410082, China;* ⓘ orcid.org/0000-0002-5667-9126

Complete contact information is available at:
https://pubs.acs.org/10.1021/acsami.1c24349

Author Contributions

G.Z. and Y.Z. conceived the idea and designed the experiment. G.Z fabricated the devices. G.Z., Y.S., M.S., and X. M. conducted the characterization measurement. Y.Z. and Y.S. directed and supervised the project. G.Z. wrote the first draft of the paper. Y.Z., B.Y., and Y.S. revised the paper. All author analyzed their data and commented on the paper.

Notes

The authors declare no competing financial interest.

■ ACKNOWLEDGMENTS

■ REFERENCES

(1) Kojima, A.; Teshima, K.; Shirai, Y.; Miyasaka, T. Organometal Halide Perovskites as Visible-light Sensitizers for Photovoltaic Cells. *J. Am. Chem. Soc.* **2009**, *131*, 6050−6051.

(2) Zheng, Y.; Huang, J.; Wang, G.; Kong, J.; Huang, D.; Mohadjer Beromi, M.; Hazari, N.; Taylor, A. D.; Yu, J. A Highly Efficient Polymer Non-fullerene Organic Solar Cell Enhanced by Introducing a Small Molecule as a Crystallizing-agent. *Mater. Today* **2018**, *21*, 79−87.

(3) Park, N.-G. Perovskite solar cells: An Emerging Photovoltaic Technology. *Mater. Today* **2015**, *18*, 65−72.

(4) Shi, B.; Duan, L.; Zhao, Y.; Luo, J.; Zhang, X. Semitransparent Perovskite Solar Cells: From Materials and Devices to Applications. *Adv. Mater.* **2020**, *32*, 1806474.

(5) Tu, Y.; Wu, J.; Xu, G.; Yang, X.; Cai, R.; Gong, Q.; Zhu, R.; Huang, W. Perovskite Solar Cells for Space Applications: Progress and Challenges. *Adv. Mater.* **2021**, *33*, 2006545.

(6) Tu, Y.; Xu, G.; Yang, X.; Zhang, Y.; Li, Z.; Su, R.; Luo, D.; Yang, W.; Miao, Y.; Cai, R.; Jiang, L.; Du, X.; Yang, Y.; Liu, Q.; Gao, Y.; Zhao, S.; Huang, W.; Gong, Q.; Zhu, R. Mixed-cation Perovskite Solar Cells in Space. *Sci. China Phys. Mech. Astron.* **2019**, *62*, 974221.

(7) Liu, M.; Johnston, M. B.; Snaith, H. J. Efficient Planar Heterojunction Perovskite Solar Cells by Vapour Deposition. *Nature* **2013**, *501*, 395−398.

(8) Wu, C.-G.; Chiang, C.-H.; Tseng, Z.-L.; Nazeeruddin, M. K.; Hagfeldt, A.; Grätzel, M. High Efficiency Stable Inverted Perovskite Solar Cells without Current Hysteresis. *Energy Environ. Sci.* **2015**, *8*, 2725−2733.

(9) Calió, L.; Kazim, S.; Grätzel, M.; Ahmad, S. Hole-transport Materials for Perovskite Solar Cells. *Angew. Chem., Int. Ed.* **2016**, *55*, 14522−14545.

(10) Chueh, C.-C.; Li, C.-Z.; Jen, A. K.-Y. Recent Progress and Perspective in Solution-processed Interfacial Materials for Efficient and Stable Polymer and Organometal Perovskite Solar Cells. *Energy Environ. Sci.* **2015**, *8*, 1160−1189.

(11) Xu, L.; Chen, X.; Jin, J.; Liu, W.; Dong, B.; Bai, X.; Song, H.; Reiss, P. Inverted Perovskite Solar Cells Employing Doped NiO Hole Transport Layers: A Review. *Nano Energy* **2019**, *63*, 103860.

(12) Yan, W.; Ye, S.; Li, Y.; Sun, W.; Rao, H.; Liu, Z.; Bian, Z.; Huang, C. Hole-transporting Materials in Inverted Planar Perovskite Solar Cells. *Adv. Energy Mater.* **2016**, *6*, 1600474.

(13) Luo, D.; Yang, W.; Wang, Z.; Sadhanala, A.; Hu, Q.; Su, R.; Shivanna, R.; Trindade, G. F.; Watts, J. F.; Xu, Z.; Liu, T.; Chen, K.; Ye, F.; Wu, P.; Zhao, L.; Wu, J.; Tu, Y.; Zhang, Y.; Yang, X.; Zhang, W.; Friend, R. H.; Gong, Q.; Snaith, H. J.; Zhu, R. Enhanced Photovoltage for Inverted Planar Heterojunction Perovskite Solar Cells. *Science* **2018**, *360*, 1442−1446.

(14) Deng, Y.; Van Brackle, CH; Dai, X.; Zhao, J.; Chen, B.; Huang, J. Tailoring Solvent Coordination for High-speed, Room-temperature Blading of Perovskite Photovoltaic Films. *Sci. Adv.* **2019**, *5*, No. eaax7537.

(15) Wang, X.; Rakstys, K.; Jack, K.; Jin, H.; Lai, J.; Li, H.; Ranasinghe, C. S. K.; Saghaei, J.; Zhang, G.; Burn, P. L.; Gentle, I. R.; Shaw, P. E. Engineering Fluorinated-cation Containing Inverted Perovskite Solar Cells with an Efficiency of >21% and Improved Stability towards Humidity. *Nat. Commun.* **2021**, *12*, 52.

(16) Xu, G.; Xue, R.; Stuard, S. J.; Ade, H.; Zhang, C.; Yao, J.; Li, Y.; Li, Y. Reducing Energy Disorder of Hole Transport Layer by Charge Transfer Complex for High Performance p-i-n Perovskite Solar Cells. *Adv. Mater.* **2021**, *33*, 2006753.

(17) Yaghoobi, N.; Méndez, M.; Paci, B.; Generosi, A.; Di Carlo, A.; Palomares, E. Analysis of the Efficiency Losses in Hybrid Perovskite/PTAA Solar Cells with Different Molecular Weights: Morphology versus Kinetics. *ACS Appl. Energy Mater.* **2020**, *3*, 6853−6859.

(18) Lee, I.; Rolston, N.; Brunner, P.-L.; Dauskardt, R. H. Hole-transport Layer Molecular Eight and Doping Effects on Perovskite Solar Cell Efficiency and Mechanical Behavior. *ACS Appl. Mater. Interfaces* **2019**, *11*, 23757−23764.

(19) Abate, A.; Leijtens, T.; Pathak, S.; Teuscher, J.; Avolio, R.; Errico, M. E.; Kirkpatrik, J.; Ball, J. M.; Docampo, P.; McPherson, I.; Snaith, H. J. Lithium Salts as "redox active" P-type Dopants for Organic Semiconductors and Their Impact in Solid-state Dye-sensitized Solar Cells. *Phys. Chem. Chem. Phys.* **2013**, *15*, 2572−2579.

(20) Snaith, H. J.; Grätzel, M. Enhanced Charge Mobility in a Molecular Hole Transporter via Addition of Redox Inactive Ionic Dopant: Implication to Dye-sensitized Solar Cells. *Appl. Phys. Lett.* **2006**, *89*, 262114.

(21) Watson, B. L.; Rolston, N.; Bush, K. A.; Taleghani, L.; Dauskardt, R. H. Synthesis and Use of a Hyper-connecting Crosslinking Agent in the Hole-transporting Layer of Perovskite Solar Cells. *J. Mater. Chem. A* **2017**, *5*, 19267−19279.

(22) Wang, Q.; Bi, C.; Huang, J. Doped Hole Transport Layer for Efficiency Enhancement in Planar Heterojunction Organolead Trihalide Perovskite Solar Cells. *Nano Energy* **2015**, *15*, 275−280.

(23) Yao, Y.; Hsu, W.-L.; Dagenais, M. High-efficiency Perovskite Solar Cell Based on Sequential Doping of PTAA. *IEEE J. Photovolt.* **2019**, *9*, 1025−1030.

(24) Kim, Y.; Jung, E. H.; Kim, G.; Kim, D.; Kim, B. J.; Seo, J. Sequentially Fluorinated PTAA Polymers for Enhancing V_{OC} of High-performance Perovskite Solar Cells. *Adv. Energy Mater.* **2018**, *8*, 1801668.

(25) Shao, Y.; Yuan, Y.; Huang, J. Correlation of Energy Disorder and Open-circuit Voltage in Hybrid Perovskite Solar Cells. *Nat. Energy* **2016**, *1*, 15001.

(26) Bi, C.; Wang, Q.; Shao, Y. C.; Yuan, Y. B.; Xiao, Z. G.; Huang, J. S. Non-wetting Surface-driven High-aspect-ratio Crystalline Grain Growth for Efficient Hybrid Perovskite Solar Cells. *Nat. Commun.* **2015**, *6*, 7747.

(27) Miyasaka, T.; Kulkarni, A.; Kim, G. M.; Öz, S.; Jena, A. K. Perovskite Solar Cells: Can We Go Organic-free, Lead-free, and Dopant-free? *Adv. Energy Mater.* **2020**, *10*, 1902500.

(28) Schloemer, T. H.; Christians, J. A.; Luther, J. M.; Sellinger, A. Doping Strategies for Small Molecule Organic Hole-transport Materials: Impacts on Perovskite Solar Cell Performance and Stability. *Chem. Sci.* **2019**, *10*, 1904−1935.

(29) Zhao, Q.; Wu, R.; Zhang, Z.; Xiong, J.; He, Z.; Fan, B.; Dai, Z.; Yang, B.; Xue, X.; Cai, P.; Zhan, S.; Zhang, X.; Zhang, J. Achieving Efficient Inverted Planar Perovskite Solar Cells with Nondoped PTAA as a Hole Transport Layer. *Org. Electron.* **2019**, *71*, 106−112.

(30) Yu, J. C.; Kim, D. B.; Baek, G.; Lee, B. R.; Jung, E. D.; Lee, S.; Chu, J. H.; Lee, D.-K.; Choi, K. J.; Cho, S.; Song, M. H. High-performance Planar Perovskite Optoelectronic Devices: A Morphological and Interfacial Control by Polar Solvent Treatment. *Adv. Mater.* **2015**, *27*, 3492−3500.

(31) Chen, B.; Yang, M.; Priya, S.; Zhu, K. Origin of J-V Hysteresis in Perovskite Solar Cells. *J. Phys. Chem. Lett.* **2016**, *7*, 905−917.

(32) Zhang, F.; Zhu, K. Additive Engineering for Efficient and Stable Perovskite Solar Cells. *Adv. Energy Mater.* **2020**, *10*, 1902579.

(33) Jiang, L.; Sun, Y.; Peng, H.; Li, L.-J.; Wu, T.; Ma, J.; Chiang Boey, F. Y.; Chen, X.; Chi, L. Enhanced Electrical Conductivity of Individual Conducting Polymer Nanobelts. *Small* **2011**, *7*, 1949−1953.

(34) Joo, Y.; Agarkar, V.; Sung, S. H.; Savoie, B. M.; Boudouris, B. W. A Nonconjugated Radical Polymer Glass with High Electrical Conductivity. *Science* **2018**, *359*, 1391−1395.

(35) Shao, Y.; Xiao, Z.; Bi, C.; Yuan, Y.; Huang, J. Origin and Elimination of Photocurrent Hysteresis by Fullerene Passivation in CH3NH3PbI3 Planar Heterojunction Solar Cells. *Nat. Commun.* **2014**, *5*, 5784.

(36) Kang, Z.; Si, H.; Shi, M.; Xu, C.; Fan, W.; Ma, S.; Kausar, A.; Liao, Q.; Zhang, Z.; Zhang, Y. Kelvin Probe Force Microscopy for Perovskite Solar Cells. *Sci. China Mater.* **2019**, *62*, 776−789.

(37) Bush, K. A.; Palmstrom, A. F.; Yu, Z. S. J.; Boccard, M.; Cheacharoen, R.; Mailoa, J. P.; McMeekin, D. P.; Hoye, R. L. Z.; Bailie, C. D.; Leijtens, T.; Peters, I. M.; Minichetti, M. C.; Rolston, N.; Prasanna, R.; Sofia, S.; Harwood, D.; Ma, W.; Moghadam, F.; Snaith, H. J.; Buonassisi, T.; Holman, Z. C.; Bent, S. F.; McGehee, M. D. 23.6%-efficient Monolithic Perovskite/silicon Tandem Solar Cells with Improved Stability. *Nat. Energy* **2017**, *2*, 17009.

(38) Zheng, Y.; Shi, W.; Kong, J.; Huang, D.; Katz, H. E.; Yu, J.; Taylor, A. D. A Cytop Insulating Tunneling Layer for Efficient Perovskite Solar Cells. *Small Methods* **2017**, *1*, 1700244.

(39) Wang, M.; Wang, H.; Li, W.; Hu, X.; Sun, K.; Zang, Z. Defect Passivation using Ultrathin PTAA Layers for Efficient and Stable Perovskite Solar Cells with A High Fill Factor and Eliminated Hysteresis. *J. Mater. Chem. A* **2019**, *7*, 26421−26428.

(40) Bagheri, Z.; Matteocci, F.; Lamanna, E.; Di Girolamo, D.; Marrani, A. G.; Zanoni, R.; Di Carlo, A.; Moshaii, A. Light-induced Improvement of Dopant-free PTAA on Performance of Inverted Perovskite Solar Cells. *Sol. Energy Mater. Sol. Cells* **2020**, *215*, 110606.

(41) Wang, Z.; Fan, P.; Zhang, D.; Yang, G.; Yu, J. Enhanced efficiency and stability of p-i-n perovskite solar cells using PMMA doped PTAA as hole transport layers. *Synth. Met.* **2020**, *265*, 116428.
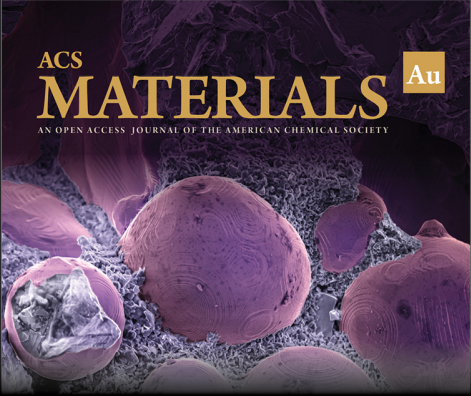
(42) Han, W.; Ren, G.; Liu, J.; Li, Z.; Bao, H.; Liu, C.; Guo, W. Recent Progress of Inverted Perovskite Solar Cells with a Modified PEDOT:PSS Hole Transport Layer. *ACS Appl. Mater. Interfaces* **2020**, *12*, 49297−49322.

(43) Qiu, L.; Zheng, X.; Zhang, J.; Yang, Y.; Cao, W.; Dong, Y.; Xia, D.; Zhou, X.; Fan, R. Insights into the Mechanism of Solid-State Metal Organic Complexes as Controllable and Stable p-Type Dopants in Efficient Planar Perovskite Solar Cells. *ACS Appl. Mater. Interfaces* **2020**, *12*, 546−555.

(44) Dong, Y.; Zhang, J.; Yang, Y.; Qiu, L.; Xia, D.; Lin, K.; Wang, J.; Fan, X.; Fan, R. Self-Assembly of Hybrid Oxidant POM@Cu-BTC for Enhanced Efficiency and Long-Term Stability of Perovskite Solar Cells. *Angew. Chem. Int. Ed.* **2019**, *58*, 17610−17615.

(45) Liu, G.; Zheng, H.; Ye, J.; Xu, S.; Zhang, L.; Xu, H.; Liang, Z.; Chen, X.; Pan, X. Mixed-Phase Low-Dimensional Perovskite-Assisted Interfacial Lead Directional Management for Stable Perovskite Solar Cells with Efficiency over 24. *ACS Energy Lett.* **2021**, *6*, 4395−4404.

(46) Zheng, H.; Wu, W.; Xu, H.; Zheng, F.; Liu, G.; Pan, X.; Chen, Q. Self-Additive Low-Dimensional Ruddlesden-Popper Perovskite by the Incorporation of Glycine Hydrochloride for High-Performance and Stable Solar Cells. *Adv. Funct. Mater.* **2020**, *30*, 2000034.